Science Advances
AAAS

Supplementary Materials for

Purcell-enhanced x-ray scintillation

Yaniv Kurman *et al.*

Corresponding author: Charles Roques-Carmes, chrc@stanford.edu; Ido Kaminer, kaminer@technion.ac.il

Sci. Adv. **10**, eadq6325 (2024)
DOI: 10.1126/sciadv.adq6325

This PDF file includes:

S1. Fabrication process of the nanophotonic scintillator (NS)

Materials:

Lutetium trichloride (≥99.99%, hydrate, Aldrich), Europium triacetate (99.9%, hydrate, Aldrich), Bismuth trinitrate (≥98.0%, hydrate, Aldrich), Ethanol (99.8%), Citric acid (hydrate, Aldrich), Polyethylene glycol (2kD Aldrich), Tetraethyl orthosilicate (98%, Aldrich), Triethoxymethylsilane (99%, Aldrich), HCl (37%, Aldrich).

For substrate, fused silica wafers (microchemical), sapphire wafers, random orientation (ESCO).

All materials were used as received.

Synthesis of Lu_2O_3:Eu-Bi sol-gel solution

The Eu-Bi co-doped Lu_2O_3 solution was prepared via a non-traditional sol-gel method where metal cations are trapped in the polymer gel, which is known as the Pechini method (50), see Fig. S1, which involves the formation of hard crystallite agglomerates. Hydrated precursors salts were dissolved separately in two different vials: (1) 0.28 gr Lutetium(III) chloride hydrate was dissolved in 6 ml Ethanol at room temperature. (2) 0.025 gr Europium(III) acetate hydrate and 0.0035 gr Bismuth(III) nitrate hydrate were vigorously stirred in water at a temperature of 70 C for 2 hrs. Water was then evaporated until reaching a volume of 0.2 ml.

The contents of the two vials were mixed, and 0.48 gr of Citric acid was added to chelate the metal ions. Then, the solution was filtered using a 0.22 micron syringe filter to guarantee a clear solution of fully dissolved metal ions. 0.14 gr Polyethylene glycol (PEG) was added to the solution, interconnecting the metal chelates via poly-esterification reaction. Finally, the solution was stirred for 2 hrs at 50 C and was found to be stable for at least 12 days.

Synthesis of SiO_2 sol-gel solution

A SiO_2 solution was prepared via conventional sol-gel methods, where metal-oxygen polymer networks are formed by hydrolysis and condensation of metal alkoxides or salts. 1.12 ml of Tetraethyl orthosilicate (TEOS) and 0.18 ml Methyltriethoxysilane (MTES) precursors were stirred and dissolved in 5.47 ml of Ethanol. Acidic solution of 0.25 ml of HCl and 0.75 ml water was added drop by drop as hydrolysis catalyst. The solution was stirred and aged for at least 1 week before usage. The gel was diluted with Ethanol in a 1:1 volume ratio 1 day before usage to reduce film thickness.

Substrate preparation, coating, and calcination

The substrates were thoroughly cleaned from all organics. Fused silica and sapphire wafers were ultrasonically cleaned (35 W) in acetone followed by isopropanol, 20 minutes each step, and blow dried under a stream of dry nitrogen. The solution was uniformly deposited onto the substrate using a spin coater (Fig. S2 central panel). All layers were spun at 2700 RPM for 30 seconds under 35-45%RH conditions. After deposition, the samples were dried and calcinated in a tube furnace in a consecutive 3-step process, under the conditions specified in table S1 (also in Fig. S2 right panel).

	Temperature (C)	Heating rate	Atmosphere
Step1	20-120	2 C/min	Ambient
Step 2	120-600	10 C/min	N_2 flow, 1000 mbar
Step 3	600-1050	15 C/min	N_2 flow, 1000 mbar

Table S1: calcination heating protocol steps

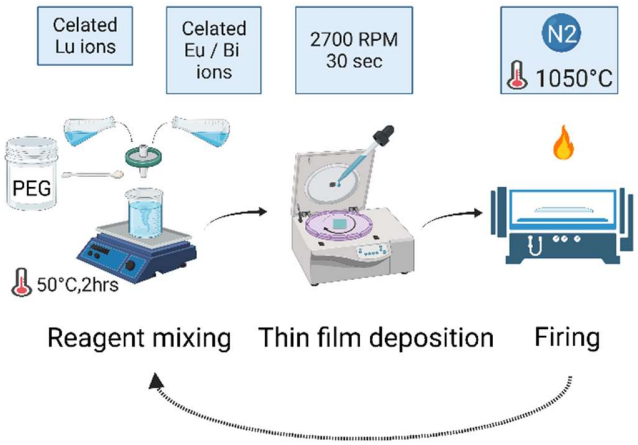

Figure S1: Schematic description of the sol gel-spin coating sample preparation method. A solution of Eu-Bi doped Lu_2O_3 is prepared by the Pechini method. The gel is distributed over a fused silica substrate via spin coating, forming a green film of metal ions trapped in a polymeric structure. The final calcination process takes place in an inert atmosphere furnace at 1050 C, where all organics are pyrolyzed and a metal oxide layer remains.

S2. Experimental setup

Anisotropic scintillation measurements

A flexible fiberoptic-based setup has been built to characterize the lateral angular emission of the X-ray-driven scintillation. The squared sample, placed vertically on an xyz-stage, was excited with X-rays on its back side while the emission has been analyzed at different horizontal angles (60° to plus 60° with respect to sample's normal direction) on the sample's front side.

For excitation, a continuous wave (CW) X-ray source (Amptek, Mini-X2 compact X-ray tube with silver transmission target and a beryllium window) has been applied at its maximum power of 10 W (with 50 kV and 200 μA). The collection area was defined by an iris, positioned between the sample and the lens. The emitted scintillation was collected at specific emission angle by a 1-inch lens, which focused the light into a tip of an optical fiber (D=0.6 mm) placed at the lens's focal plane (f=150 mm) on its optical axis. This arrangement ensures that only light from the iris selected area on the sample and parallel to the optical axis of the lens is collected and conducted by the flexible fiberoptic to the spectrometer (Acton SpectraPro-150) equipped with a sensitive EM-CCD camera (Andor iXon ultra). Whereas the camera electron-multiplying (EM) regime was turned off during the measurements.

The entire collecting optical set (iris, lens, and the optical fiber's tip) has been aligned along a rotating rail (RLA300/M, Thorlabs) mounted under the sample on a motorized continuous rotation stage (Thorlabs, PRMTZ8), with its rotational axis grazing the sample's frontal surface. For the angular measurements, the sample's orientation remained fixed, while the entire optical rail rotated horizontally facing the sample's surface under an angle in respect to its normal (surface's normal defined as 0°) enabling angular emission measurements. The theoretical angular

uncertainty induced by the 0.6 mm fiber diameter over 150 mm focal length is 0.23°. Even considering possible alignment inaccuracies, the analyzed angular resolution is still better than 1°.

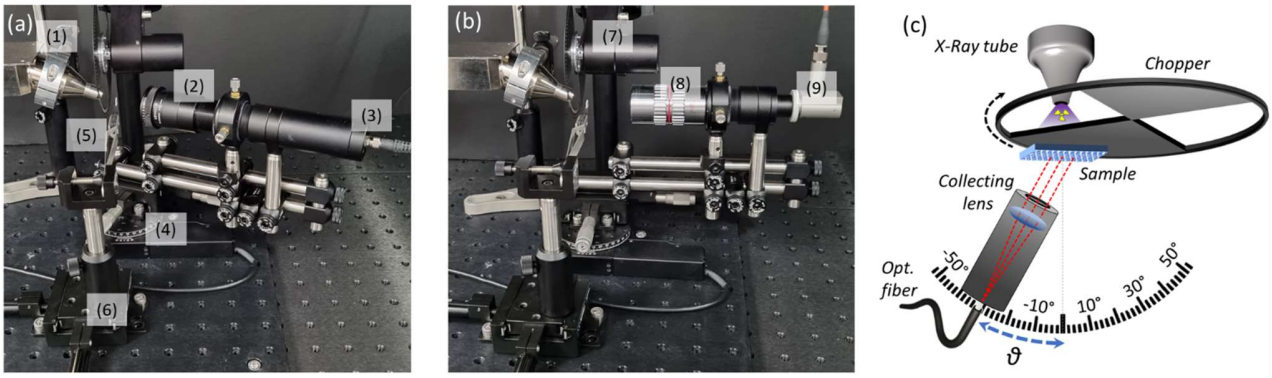

Figure S2: Detailed description of the scintillation experimental setup. (a) For the angular light yield measurements, the components include: (1) A continuous wave X-ray source, (Ag, 50 kV, 10 W); (2) Iris followed by a lens (F=150 mm) aligned along the optical axis to (3) the tip of the optical fiber in the focal plane that collects only parallel emitted light from the sample's area as defined by the iris. The entire optical tube is held by (4) a rotational stage with the optical axis aligned to cross the rotational axis exactly at (5) the sample's surface. The sample is mounted on (6) a motorized translational stage. **(b)** For time response measurements, (7) a metallic chopper blade is placed between the X-ray tube and the sample. Then, the lens is replaced by (8) an objective focused on the sample along the optical axis. The emitted light is finally collected by a (9) parabolic mirror into an optical fiber. **(c)** A schematic illustration of the experimental setup.

Time-response measurements of anisotropic scintillation

For achieving temporal measurements, an optical chopper (MC1F2, Thorlabs) was installed between the X-ray tube and the sample. The metal chopper blade was rotated at a frequency of 80 Hz. Due to low signal-to-noise ratio, we have also modified the light collecting setup compared to the previous section. The iris, which previously defined the area of interest on the sample while collecting light emitted in the parallel direction only, was now replaced by an objective (0.14 NA, Motic, Plan APO, ELWD 5x/0.14, WD=34 mm), which collects the light from a small focal spot but also from a wider emission angle of about 16°. The previously used lens and the 0.6 mm fiber optic have been exchanged with a parabolic mirror which focused the parallel

light into a 0.1 mm fiber. The exchange of the later was done for connection compatibility of the optical fibers to the single-photon avalanche diode detector (PDM photon counting series), which were used for the temporal measurements. The detector and chopper were synchronized by a Time Tagger (Swabian Instruments, Time Tagger Ultra, 1.2(1) hardware) to collect single photons into a time-dependent histogram.

Photoluminescence experimental setup

The ultraviolet (UV)-induced emission and excitation spectra were recorded at room temperature using Edinburgh instruments FLS1000-xS-t Fluorescence Spectrometer. The front of the samples was excited at an angle of 45 degrees by Xe lamp with a 4 nm wide scan slit centered at 375 nm wavelength. The signal was collected at 45 degrees and recorded in 0.1 nm resolution via PMT detector. The UV luminescent dynamics were investigated using variable pulsed diode laser (VPL)-375 nm source set to a 1 μs pulse duration and 40 Hz repetition rate. The signal was collected at the angles of 0, 30, and 45 degrees. Collection angles of 30 and 45 degrees took place inside the chamber, having 90 degrees between the excitation source and the detector. Measurement at 0 degree was taken using Nikon Eclipse Ni-U upright microscope, using 10X objective with 0.3 NA. The emitted photons were collected at the same angle of excitation by using a 414 nm dichroic mirror, coupled to an optical fiber into the detector. long-pass filter of 395 nm was positioned after the collecting lens.

Scanning electron microscope

A Zeiss Gemini 500 high-resolution scanning electron microscope (SEM) was used at an accelerating voltage of 5 and 20 kV for surface topography modeling, elemental distribution mapping, and identification of emission centers. We also executed imaging with the SEM secondary electron (SE) and energy-dispersive spectroscopy (EDS) using the Bruker

XFlash/60mm. Electrons accelerated to 5 keV were also used to induce cathodoluminescence (CL), collected via parabolic lens using the Gatan MonoCL4 Elite detector and spectrometer. Dispersion grating was set to a maximum of 1200 lines/mm to collect the maximum spectrum width and a 1 mm slit, giving a 2.7 nm spectral resolution.

Atomic force microscopy (AFM)

The samples thickness and surface were analyzed by AFM and a fluorescence confocal optical microscope (Nikon Eclipse Ni-U upright equipped with a DFK 23UP031 camera), using 40X objective with 0.75 NA. The fluorescence microscope micrographs were obtained by illuminations under white light and by a narrow band Xe lamp, centered at 375nm. AFM tapping mode images were taken from an area of 5×5 μm^2 to model surface topography. An additional optical examination of the samples was captured by the AFM optical Brightfield Microscope.

X-ray diffraction (XRD)

XRD analysis was performed to identify the formation of different material phases. The XRD patterns of the samples were obtained by Rigaku Smart-Lab 9 kW high-resolution X-ray diffractometer. We used the general, medium resolution parallel light (PB) operation package with a monochromatized Cu target radiation source (λ = 1.54 Å).

S3. Materials characterization

In this section, we explain how we extracted the optical properties of the materials in the multilayer scintillator (their refractive indices and absorption coefficients), as well as estimating optically the physical thickness of a single film of each material. The film thicknesses and refractive indexes were used as a base for the nanophotonic scintillator (NS) optical design. The optical measurements, which include the reflection and transmission spectra, were done in a spectrophotometer (Agilent carry 5000 UMA). The reflection spectrum was taken solely from the front surface, by oil matching the back surface with a wedge to divert its reflection.

To extract the optical properties of the materials, we have analyzed the optical spectra of a single homogeneous thin film at a time which was deposited onto a high contrast substrate: random orientation Sapphire for SiO_2 (Fig. S3a) and Fused silica for Lu_2O_3 (Fig. S3b). From the front surface reflection spectra of the substrate, its refractive index n_s as a function of wavelength λ was calculated according to

$$n_s(\lambda) = \frac{1+\sqrt{R_f(\lambda)}}{1-\sqrt{R_f(\lambda)}} \tag{S1}$$

where R_f is the reflection spectra, collected only from the film side of the sample. By having the substrate refractive index, we can extract the refractive indices of a thin layer n_f that is stated on top of the substrate from local extremum points λ_{ext} according to

$$n_f(\lambda_{ext}) = \sqrt{\frac{n_s(\lambda_{ext})\left(1+\sqrt{R_f(\lambda_{ext})}\right)}{1-\sqrt{R_f(\lambda_{ext})}}}. \tag{S2}$$

The physical thicknesses of the layers are calculated from the optical thicknesses according to

$$d = m\frac{\lambda_{ext}}{4n_f} \tag{S3}$$

where m can be any integer. Then, the absorption coefficient α of the layers was calculated as a function of wavelength from the reflection and transmission spectra, including both side of the sample

$$\alpha = \frac{1}{d} ln \frac{100 - R}{T} \tag{S4}$$

(derived from Lambert's law and normalized by the thickness).

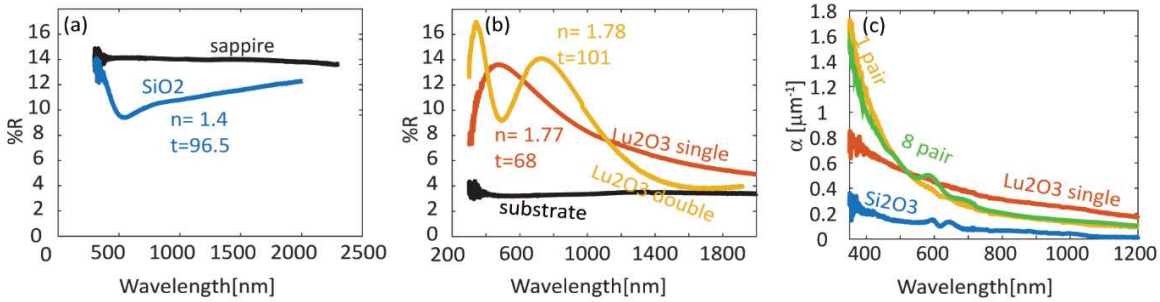

Figure S3: Single-layer optical characterization. (a) Optical characterization of a single SiO_2 layer deposited onto a Sapphire substrate. From the spectral analysis, we calculated the refractive index to be ~1.4 and the layer thickness to be ~96.5 nm. **(b)** Optical characterization of a single and a double Lu_2O_3 layer deposited onto a Fused silica substrate. From the spectral analysis, we calculated the refractive index to be ~1.8 and the layer thickness to be ~65 nm for a single layer and ~100 nm for a double layer (when repeating a single-layer fabrication step twice). **(c)** The extracted absorption coefficient of the layers α [μm^{-1}] was calculated for each wavelength using Eq. (S4). Single layers of SiO_2 (blue) show relatively low absorption compared to a single Lu_2O_3 layer (orange). We also find that one pair of a SiO_2 layer and a double Lu_2O_3 layer (yellow) and the 8 pairs structure (green) show similar absorption behavior.

Using the method above, we calculated the refractive indices and thicknesses of the materials. We find that our SiO_2 layer has a refractive index of ~1.4 at the minimum point of 540 nm, and a physical thickness of ~96.5 nm, while the refractive index of a single layer of Lu_2O_3 was estimated to n=1.77 at 475 nm and a thickness of 68 nm. Importantly, since we were aiming to reach a thicker Lu_2O_3 for stronger scintillation, we doubled the Lu_2O_3 deposition process for each layer. According to a similar analysis, the double-layer Lu_2O_3 had a refractive index of 1.78

at 724 nm and thickness of 101 nm. The calculated absorption coefficients of the materials are shown in Fig. S2c. We find that the stacking of the layers generates an additional scattering mechanism, and that the scaling from a single pair to 8 pairs does not add additional scattering effects as the two plots overlap. This analysis is thoroughly discussed in section S.8 below.

Since the thicknesses of each layer has a significant optical effect over the multilayer structure, we further verified layer thickness via an atomic force microscopy (AFM) measurement (Neaspec), shown in Fig. S4. The AFM line scan over a scratch was used to measure the step size to evaluate film thickness. As the scratching resulted in material pileups, two linescans were taken: one inside the scratch and the other within a certain distance from it. Using this method, a single SiO_2 layer was measured to have a 100±3.3 nm thickness and the double Lu_2O_3 layer was measured to have a thickness of 90 ± 2.3 nm.

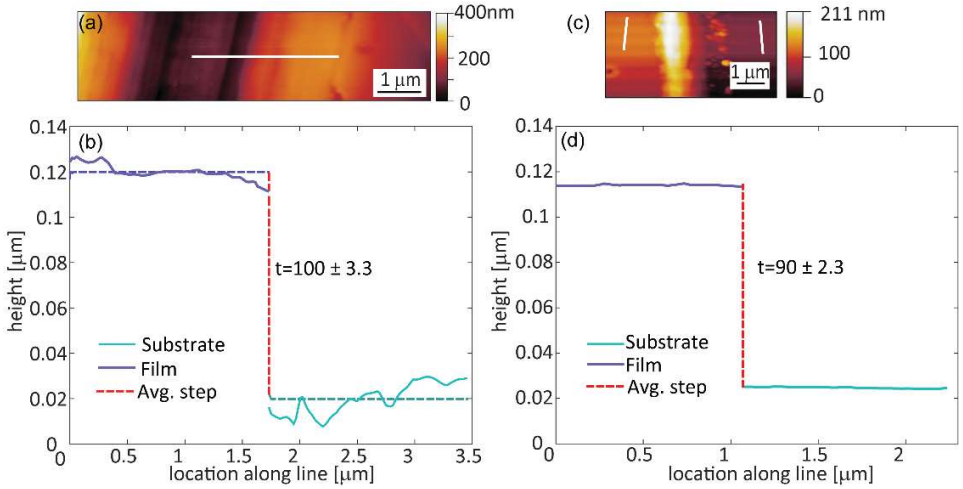

Figure S4: Single-layer AFM characterization. (a) Topographic image of a single Lu_2O_3 layer, extracted from an AFM tapping mode 8×1 μm^2. **(b)** A step measurement over a scratched. The average thickness of the step between two lines was calculated as 100 nm, supporting the thickness calculations from the optical spectrum. **(c)** Topographic image of a single SiO_2 layer, extracted from an AFM tapping mode. **(d)** The average thickness of the step between two lines was measured to be ~90 nm and close to the optical spectra calculations.

S4. Structures Characterization

The first analysis of the multilayer structure was optical spectroscopy, shown in Fig. S5. Reflection and transmission spectra were taken at different angles and verified the formation frequency of the photonic band gap, where reflection coefficient is maximized. As expected, as the angle increases, the photonic bandgap is blue shifting to shorter wavelengths. Moreover, at 30 degrees (green line) the band-edge of the NS, where emission rate is maximized, is aligned with the Eu+3 emission peak at 612 nm (dashed line). Therefore, this reflection measurement further proves that the emission enhancement at 30 degrees, shown in the main text, is caused by the optical response of the NS and not from scattering.

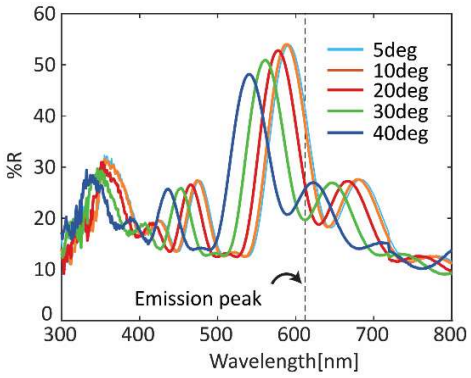

Figure S5: Multilayer optical characterization. Reflection spectra of the 8 pair NS at different detection angles. The 612 nm emission band peak (dashed line) is aligned with the bandgap edge at the detection angle of 30 degrees (green), therefore is expected to have enhanced intensity at this angle.

Apart from the optical characterization, we can compare the X-ray scintillation signal that we present in the main text to the emission in photoluminescence (PL) and cathodoluminescence (CL), shown in Fig. S6b,c that is in agreement with the electronic band structure shown in S6a. We compare the emission from the NS with a Lu_2O_3 sample having the same amount of scintillating material (that we refer here as a bulk).

From the homogeneous sample CL (Fig. S6b) and the PL we can detect sharp peaks of the main 5D→7F2 transition at 612 nm, as well as many secondary transitions at 580 nm, 587 nm, 593 nm, 600 nm and 632 nm and few smaller peaks are also apparent between 680 to 713 nm. We find the scintillation emission is much wider in energy, which may be also attributed to our lower scintillation spectral resolution that occur due to a misalignment between the grating and the CCD camera and to low coupling between the fiber optics and the detector.

In the NS sample (Fig. S6c), the PL signal has similarities to the homogeneous sample response, while the scintillation and CL of the NS show stronger secondary transitions. These differences lie in the luminescence mechanism, PL excitons are localized while CL and scintillation involve spatial transportation of electrons. In the scintillation process, the energy is absorbed in the Lu_2O_3 layer, but the ejected electrons transfer some of the energy to the interface between Lu_2O_3 and SiO_2 layers. At the interfaces between the layers, the sample is expected to experience thermal stress, formation of new silicate phases due to the diffusion of ions, and internal fields. All these mechanisms are expected to create perturbation and inhomogeneous broadening of the emission spectra (51). These deviations are dominant in the CL spectrum, where the electrons energy is mainly absorbed at the first interface from the top.

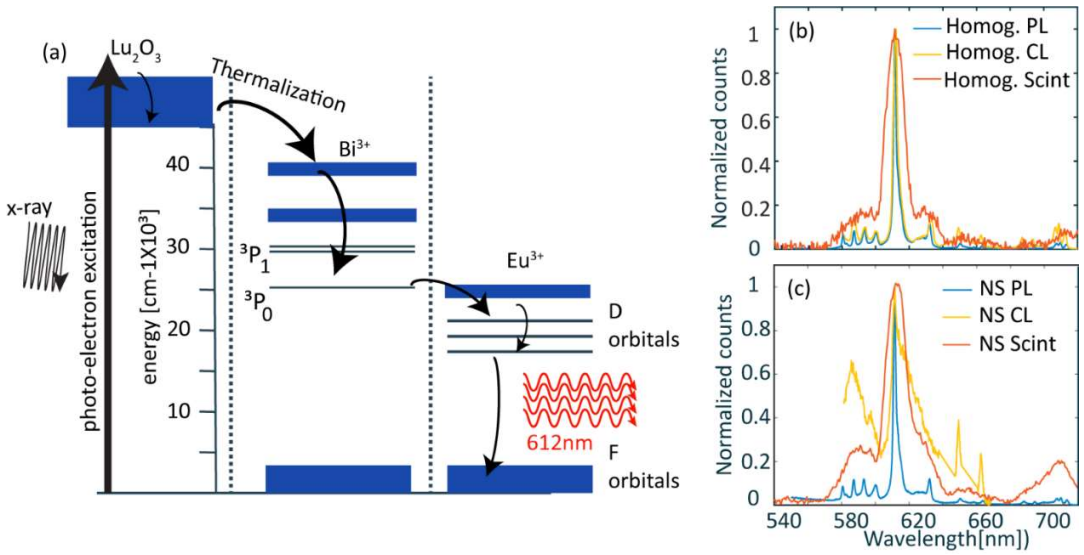

Figure S6: Energy level diagram and the corresponding photoluminescence (PL), cathodoluminescence (CL), and X-ray scintillation spectra. (a) Energy level diagram showing energy transfer between Bi and Eu ions in a co-doped Lu_2O_3 host matrix. The high X-ray energy is absorbed by the Lu_2O_3 host via a photo-electron, which then thermalizes to the Bi ion traps and then passes to the Eu ions where a radiative 612-nm recombination takes place. **(b-c)** We find that the homogeneous sample(b) keeps its emission properties between excitations while the NS emission (c) has a significant deviation between the excitations due to the different energy transport inside the structure.

XRD analysis was used for investigation of the phases formed in the samples. Fig. S7 confirms the formation of a cubic phase Lu_2O_3 structure by its good agreement with The Powder Diffraction File of the International Centre for Diffraction Data (JCPDS 00-012-07281). The NS sample analysis indeed validates the formation of new phases and thermal stress, by showing a more complex diffraction pattern. The shifting of the distinct cubic phase, marked by red stars, can be easily explained by the compressive thermal stress between the layers. The new peaks, marked in blue, are attributed to the formation of different silicate phases (such as LSO monoclinic phase JCPDS 00-041-0239) at the layer interface, which might also shift and split under stress.

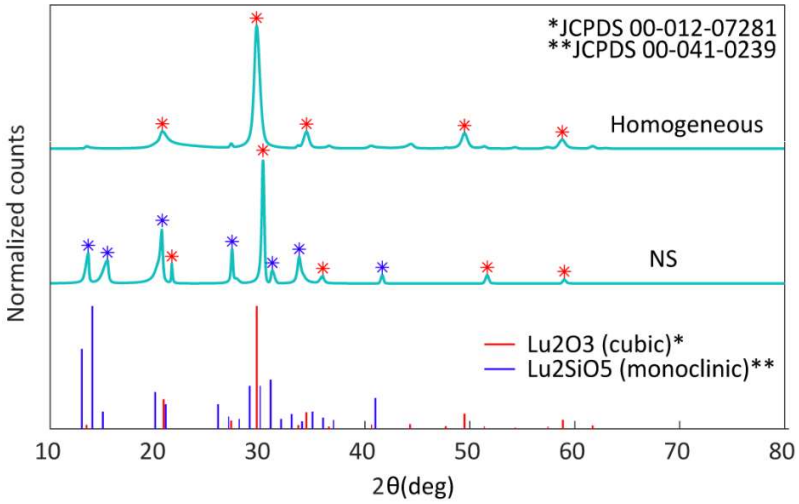

Figure S7. XRD analysis for the homogeneous and NS samples, in comparison to the literature. The bulk sample shows good alignment with cubic Lu_2O_3 phase peaks. The NS diffraction peaks are shifted with respect to literature values due to the formation of thermal stress. New peaks are also apparent for the NS samples, which could be attributed to the formation of intermediate silicate phase at the interfaces between the layers.

Topographical features of the NS and the homogeneous sample were further investigated using AFM, optical microscope, and SEM analysis. From this analysis, detailed below, we find that the fabricated structures have rough surfaces with many structural defects. In SM section S.8, we show how we analyze the influence of these features on the scintillation properties. The AFM measurements, shown in Fig. S8, reveal that the SiO_2 outer layer of the NS is porous, with a typical pore diameter of ~100nm (Fig S8d) and averaged surface roughness of 12.5nm (Fig S8b). The homogeneous Lu_2O_3 layer measurement shows a low aspect ratio surface (Fig S8c) with an overall higher surface roughness of 19.43 nm (Fig S8a). According to the absorption coefficients in Fig. S2c, the contribution of the SiO_2 pores was much smaller to the scattering than the Lu_2O_3 layer surface roughness. The Lu_2O_3 layer rough nanoscale topography can be assumed to be responsible for scattering of the short wavelengths.

It is also insightful to perform an optical comparison of the NS optical features under white light illumination and a Xe-375 nm source illumination (Figs. S8e,f, respectively). In the optical micrograph (Fig. S8e), we find that the overall thickness varies locally through the change of the observed color. In addition, we find features that scatter the white light which seem black in the image. These features include cracks, caused by the tensile stress formation in the film, clusters and chain like topographic features in the film. Under 375 nm UV illumination, all these scattering features are brighter. We suggest that these features are additional out-couplers of the light that is emitted within the sample.

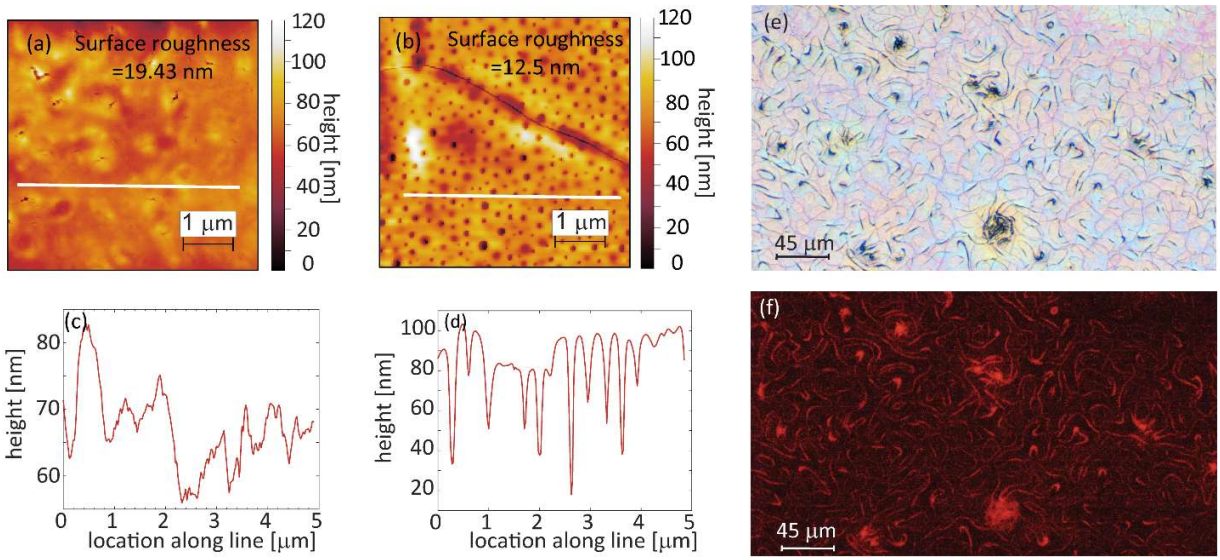

Figure S8. Surface characterization of homogeneous sample and the nanophotonic scintillator. AFM tapping mode topographic images on an area of 5×5 μm^2 and a corresponding height profiles of the **(a,b)** homogeneous sample and the **(c,d)** photonic multilayer structure. Surface roughness are evaluated as 19.43 nm and 12.5 nm for the bulk and NS respectively. **(e,f)** Fluorescence microscopy images of the NS under white light (e) and Xe-375 nm source illumination (e), showing surface structure in large scales.

Additionally, SEM, CL, and EDS mapping were used for further investigation of our scintillator's properties. The advantage of the SEM analysis over the AFM is its large field of view which enabled us to view micro-scale features. Fig. S9a is a SEM micrograph of the homogeneous scintillator, revealing a rather rough microstructures, abundant with craters. These craters are formed during calcination, as the organic materials are pyrolyzed simultaneously with the crystallization process. The continuous one step process leads to high crystallization temperatures, low nucleation density and large grains. By looking at the film channeled microstructure, one can assume that the grain growth and coalescence was either not yet completed or that a dewetting process had started to take place (52). When stacking a second layer on top, one can expect the craters will be smoothened by the top layer, leading to reduction in surface area per thickness. When zooming in the SEM image, in Fig. S9b, we can see nanoscale features of the scintillator surface. Importantly, in Fig. S9c we present the CL mapping image of Fig. S9b which shows no correlation between the emission locations, which are fairly homogeneous, and the craters. Lastly, the SEM micrograph of the NS SiO_2 top layer (Fig. S9d) smoothen the rough structure of the Lu_2O_3 layer underneath. This figure can explain the lower surface roughness of this sample, measured via AFM.

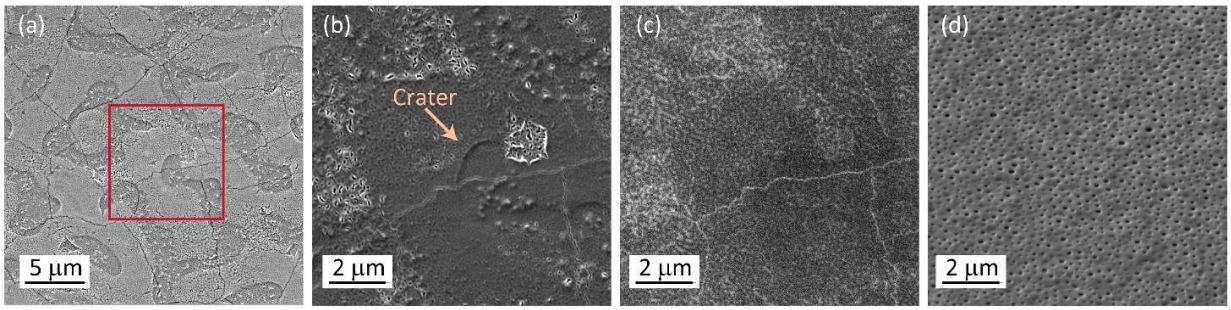

Figure S9: **SEM Secondary electrons (SE) surface topography and CL mapping. (a)** large-area micrograph of the homogeneous sample, showing top layer topography. **(b)** Higher magnification of the red square in (a), showing a clear crater and other surface imperfections. **(c)** CL mapping of the surface in (b), showing mostly homogenous emission from all the area. **(d)**

Micrograph of the NS surface, showing a different topography than the homogeneous sample. In this case, the multilayer smoothening the craters through introduce a porous surface.

In order to investigate the concentration of the emitting elements in our sample, a time-of-flight secondary ion mass spectrometry (TOF-SIMS) were acquired from an area of 100×100 μm^2, shown in Fig. S10. In Fig. S10a, the Lu, Eu and Bi, depth profiles were acquired by from the homogeneous sample, showing concentrations of 92.5, 5.2 and 2.3% atom, respectively. From a 16-multilayer NS (Fig. S10b), depth profiles of Si, Lu and Eu elements were further acquired. Although the TOF-SIMS is not sensitive to a sharp transition between layers, the measurement shows the alternating structure of a conventional scintillator (Lu_2O_3 doped with Eu) and dielectric (SiO_2). The TOF-SIMS measurements were operated under dual beam mode, where the O_2^+ (2 keV) serves as the sputtering beam with a crater size of 500×500 μm^2 and the Bi^+ (25 keV) as the analysis beam.

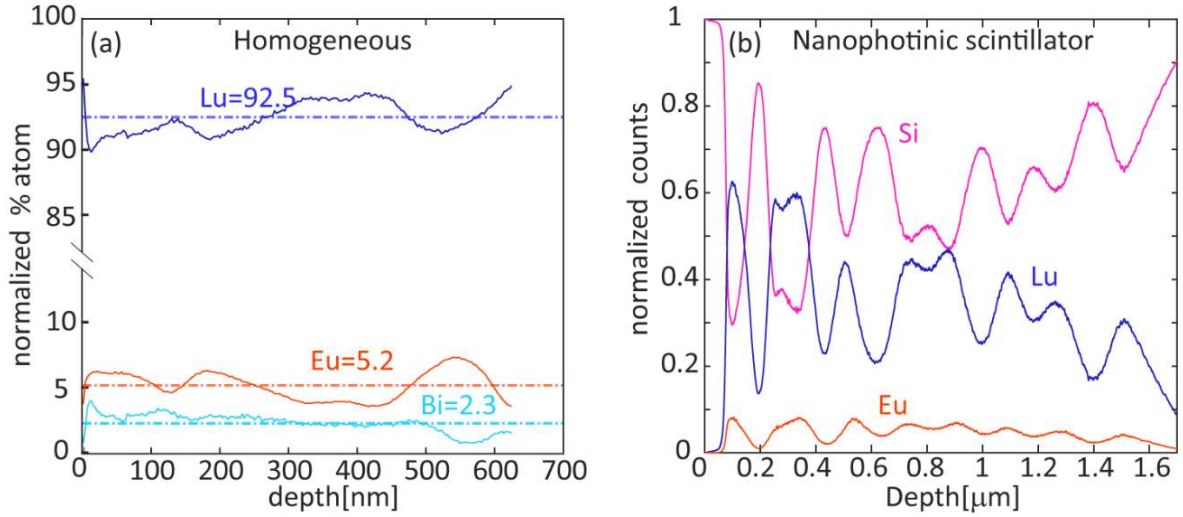

Figure S10: **TOF-SIMS depth profiles.** (a) Concentration profiles of Lu, Bi and Eu elements along the depth of Lu_2O_3:Eu,Bi layer deposited on dielectric SiO_2. The sample was measured in XPS and used as calibrated sample for the NS; The concentration is normalized to the total 100% atom of Lu, Eu, and Bi elements. (b) Depth profiles of Si, Eu, and Lu along a 16-multilayer NS structure.

S5. Analysis of scintillation decay times

Under UV excitation

We used a commercial photoluminescence (PL) instrument (Edinburgh) to extract the decay times time decay of the two structures in different angles. Although the excitation is in the UV range rather than X-rays, the spontaneous emission should be enhanced in the exact same manner because the spontaneous emission is incoherent with the excitation mechanism in both cases. Therefore, we want to first examine the reduction of the lifetimes in the NS (the Purcell effect) under UV illumination.

The normalized measurements are shown in Fig. S11 in linear and log scale, included their fit to a single exponent, using the fit $ae^{-t/\tau}$. The decay timescales are marked on each measurement. We can see that the NS has successfully improved the spontaneous emission rate of the structure (by a factor of between 1.3 to 1.5). Moreover, the NS has an angular dependency, while the homogeneous sample has a similar emission rate for the two angles that were examined. Therefore, we can say that the Purcell effect is clearly seen in the NS under the UV excitation.

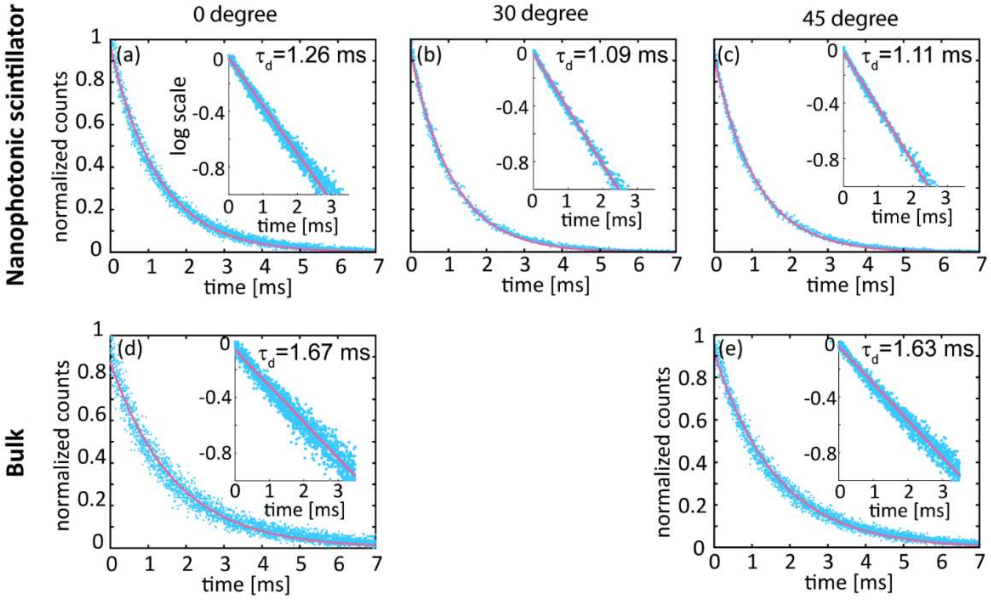

Figure S11: Decay times under UV illumination. The normalized number of counts that are emitted by the NS (a-c) and the homogeneous sample (d-e) as a function of time and angle of emission, following a UV illumination. We find a reduced decay time τ_d in the NS which indicates that the Purcell effect indeed occurs in the structure. Moreover, we observe an angular dependency for τ_d, as expected from the theory presented in Fig. 2 in the main text. In contrast, in the homogeneous sample, we find similar decay times in the two examined angles. The timescale error is 0.01 ms.

Under X-ray excitation

X-ray-pumped scintillators are an excellent platform to observe the physics of many emitters distributed over a large volume compared to the wavelength (since, for reasonable x-ray energies, the mean penetration depth in many materials is at least tens or hundreds of microns). The experimental setup is constructed by a continuous wave (CW) X-ray excitation with a chopper that blocks a large portion of the X-ray from reaching the sample. The chopper has two states. Open state: the X-rays fully passes. Closed state: a small non-zero portion of the X-ray still reaches the sample. To enable extracting the decay time, we first note that for an immediate transition between the two states, the measured open-to-closed scintillated signal gets the following form:

$$S(t) = S_c\left(1 - e^{-\frac{t}{\tilde{\tau}_d}}\right) + S_o e^{-\frac{t}{\tilde{\tau}_d}} = S_c + (S_o - S_c)e^{-\frac{t}{\tilde{\tau}_d}}, \quad \text{(S5)}$$

where S_o is the 'open' steady-state signal and S_c is the 'closed' steady-state signal. $\tilde{\tau}_d$ is the decay time until reaching the 'closed' steady-state. Importantly, $\tilde{\tau}_d$ do not depend only on the scintillator decay time, but also depend on S_o and S_c.Assuming we are looking at all the emitters in the sample as an ensemble, the probability of a single emitter to be on the excited state is 1 is when the chopper is open, but it is not 0 when the chopper is closed. Therefore, the decay time $\tilde{\tau}_d$ is smaller than the scintillation decay time τ_d since the dopant population is not zero in the 'closed' state. $\tilde{\tau}_d$ relates to the time that takes an emitter to go from being excited with 100% certainty to being excited

with $100 \times S_c/S_0\%$ certainty: a shorter time than the decay time of the UV measurement that decays to zero.

We can measure the exact ratio S_c/S_o according to the scintillation in both states (open and close) using a reference sample with an immediate response (i.e., a much faster scintillation decay times relative to all the other timescales). We chose LYSO as such a sample because it has a spontaneous emission timescale of 20 ns, where we did not measure directly the light yield of the LYSO sample, but instead used it as a reference and for calibration. The LYSO measurements served to measure the temporal response of our time-decay apparatus due to it practically immediate response compared to other time responses of the apparatus (in the ms timescale). The result, shown in Fig. S12a, show that the normalized final state ratio is 0.145. This means that a randomly chosen emitter has a probability of 0.145 to be in the excited state when the chopper is in the closed mode, and therefore X-ray scintillation decay times that we will extract for the samples of interest should be corrected.

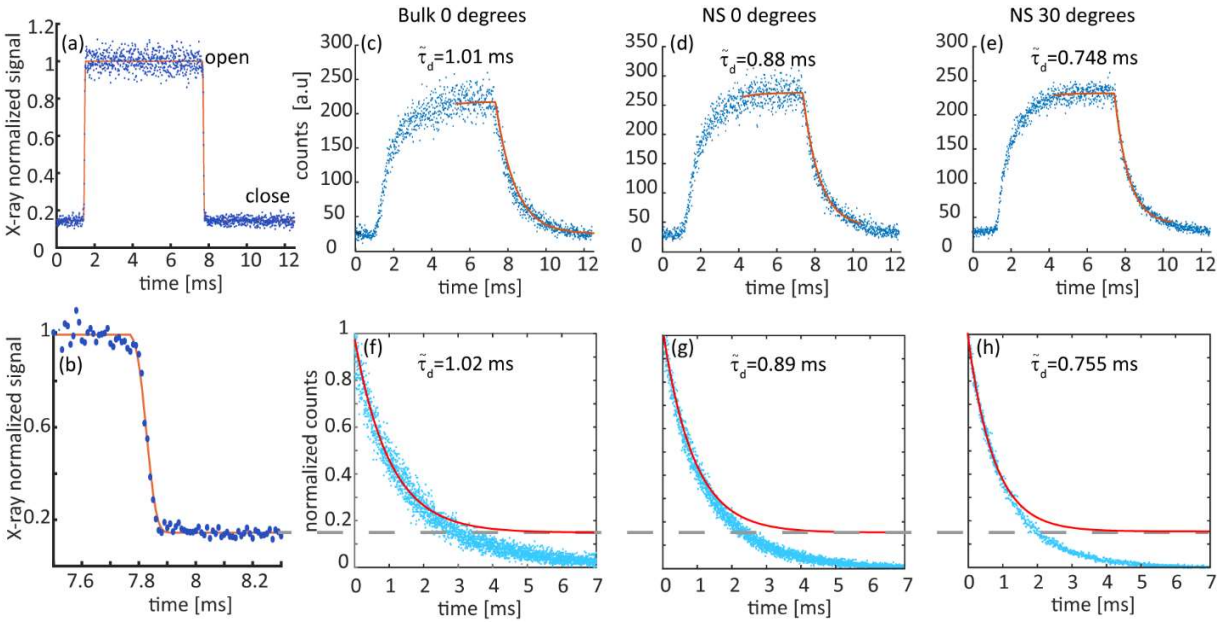

Figure S12: Extraction of X-ray scintillation lifetime and their corresponding fit to the PL measurements. (a) The X-ray temporal signal within a single chopper cycle, extracted from the

scintillation signal of a LYSO reference sample which has a time response of 20 ns, much shorter than the timescales of the chopper. From this measurement, we extract the amount of X-rays signal that pass the chopper in the close mode, 0.145. **(b)** zoom-in of (a), showing a non-immediate transient from the open to close chopper mode. **(c-e)** The scintillated signal from the homogeneous sample (c) and the NS (d-e) structures during a period of the chopper. We extract the decay times, $\tilde{\tau}_d$ (mentioned within plots), from this measurement by the best fit to Eq. (S6), where $S_{\mathrm{X-ray}}(t)$ is the signal in (a). **(f-h)** The PL signal, taken from Fig. S11, with a fit of the first 2-ms signal to an exponential decay that is forced to decay to 0.145. The decay times that we find using this method are similar to the ones extracted from the X-ray scintillated signal. Therefore, we can say that under both X-ray and UV illuminations the decay times are similar (real decay times in Fig. S11), and that the Purcell effect occurs during the scintillation process.

From the LYSO measurement, we extract another important behavior of our system, which is the transient of the chopper between its two states (Fig S12b). Since the transition between the two states in not immediate, the scintillation measurement is in fact a convolution between the sample's exponential decay and the response of the chopper that describes the X-ray signal that arrives to the sample. Therefore, we extract from the LYSO measurement the X-ray signal that arrives to the sample, $S_{\mathrm{X-ray}}(t)$. Since each X-ray photon creates scintillated light with temporal response of an exponential decay, the measured scintillation from our sample should take the form of:

$$S(t) = S_{\mathrm{X-ra}}\ (t) * e^{-\frac{t}{\tilde{\tau}_d}} \tag{S6}$$

where the symbol "$*$" describes a convolution.

Our measurements of the X-ray scintillation signal $S(t)$ are shown in Fig. S12c-e. For each one of the measurements, we extract $\tilde{\tau}_d$ using Eq. (S6) and the X-ray signal. Now, as explained above, these decay times are not the spontaneous emission rate. However, we can take the UV data and show that the decay times from the X-ray measurement are similar to the decay times from the UV illumination signal, when the signal decays to 0.145 (the probability of being in the excited state when the chopper is in the closed state). We extract these decay times by fitting the function

$f(t) = (1 - 0.145)e^{-t/\tilde{\tau}_d}$ to the first 2 ms of UV data, shown in Fig. S12f-h. The decay times found from this fit have a very good match with the decay times that we extracted in the X-ray data. Therefore, we can say confidently that the Purcell effect is shown in both the UV and X-ray excitation, and that the spontaneous decay times are independent of the excitation mechanisms.

S6. Scintillation from an ensemble of structures

In this section, we show how the angular dependence of the Purcell effect arises from the emission from an ensemble. This is demonstrated through the simulation of a simplistic structure, already exhibiting angular features. In the emission from a single emitter and/or from an ensemble of emitters, nanophotonic patterning can induce an angular dependence of the emission intensity. However, the emission rate as a function of angle is angle independent for the case of a single emitter. It can display angular dependence for the case of an ensemble of emitters. For a single emitter (or dipole) in a homogeneous media, the spontaneous emission rate is independent of the dipole orientation. However, this symmetry is disrupted when the emitter is placed within a multilayer structure that is on the scale of the optical wavelength. In such a scenario, the isotropic symmetry is no longer maintained. Instead, the rate of emission can be enhanced in different ways for emitters with different dipole orientations (because of the polarization dependence of the LDOS). This is due to the interplay between the emitter and its surrounding environment, which can cause the emission pattern to become dependent on the dipole orientation and location in space, as we show in Fig. S13. The influence of the spatial distribution of emitter is also displayed in Fig. S13 by considering dipoles at different depths in the multilayer scintillator.

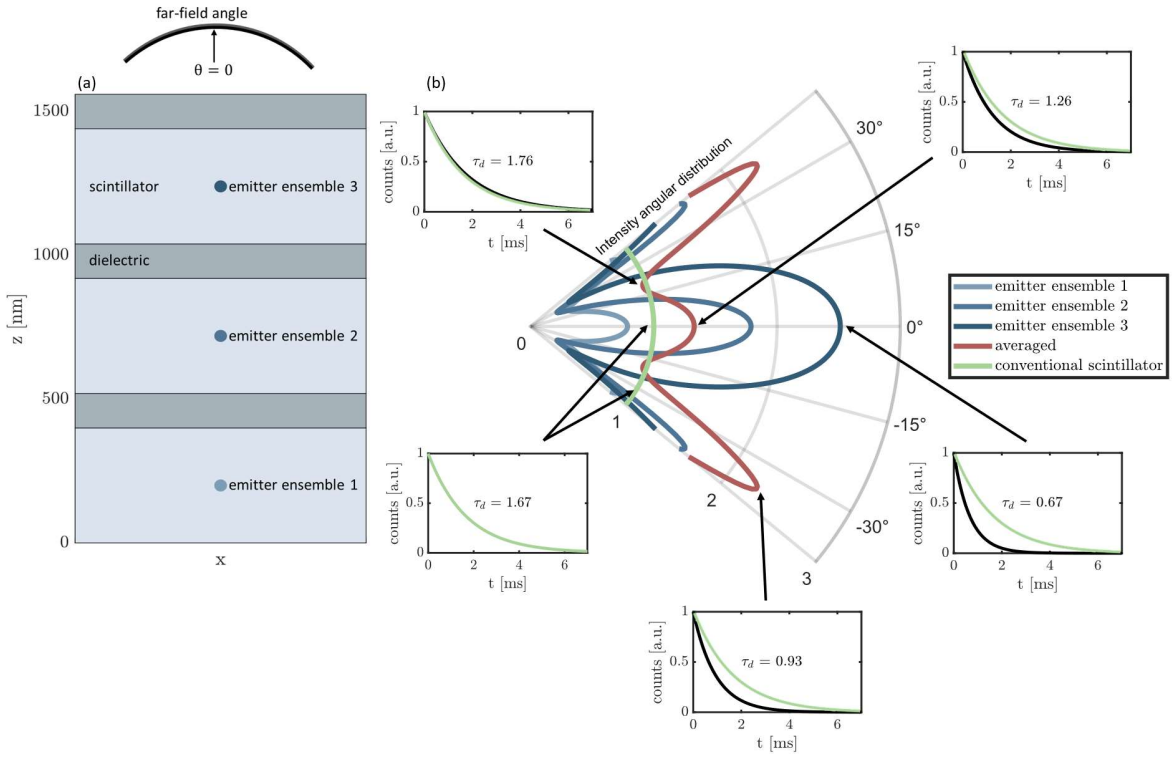

Figure S13. Simulation of the angular Purcell effect, showing that it is only possible from an ensemble of emitters and impossible from a single emitter. (a) Illustration of the multilayer structure containing three pairs of layers. The presented uniformly-oriented emitter ensembles are located at the center of each scintillator layer. We compute the emission rate enhancement of each optical mode, described by the light reaching the detector with a solid angle of θ. **(b)** The spontaneous emission rate enhancement of each emitted mode from an ensemble of emitters. The red curve is the average over the entire volume of the structure.

Moreover, we explain in this section how we incorporate the effects of variance in the parameters of the NS. When the light emission is collected from a large area, we can consider an ensemble average of structures, by treating the permittivity of the materials and the thicknesses of the layers as random variables.

We investigate the effect of uncertainty in epsilon and layers thickness by calculating $F_{p,\mathrm{eff}}(q)$, shown in Eq. (2) of the main text, for a large set of different structures. We use a normal distribution with a mean value of layer thicknesses and permittivities according to the expected fabrication properties. Fig. S14 presents tests of a range of variances, and for every variance

value, 50 different random structures are averaged, to estimate an overall Purcell factor $F_p = \int F_{p,\text{eff}}(q)dq$. The mean value of F_p and its normalized standard deviation are presented in Fig. S14. Surprisingly, our results show that the mean value is rather robust under fabrication errors. Nevertheless, the variance of the Purcell factor itself also increases for larger variance values, which can create a large reduction in the signal in some structures. Interestingly, these results show that the periodic structure is not optimal (relative to the large space of aperiodic NS), as a variance in the fabrication can often *improve* the response.

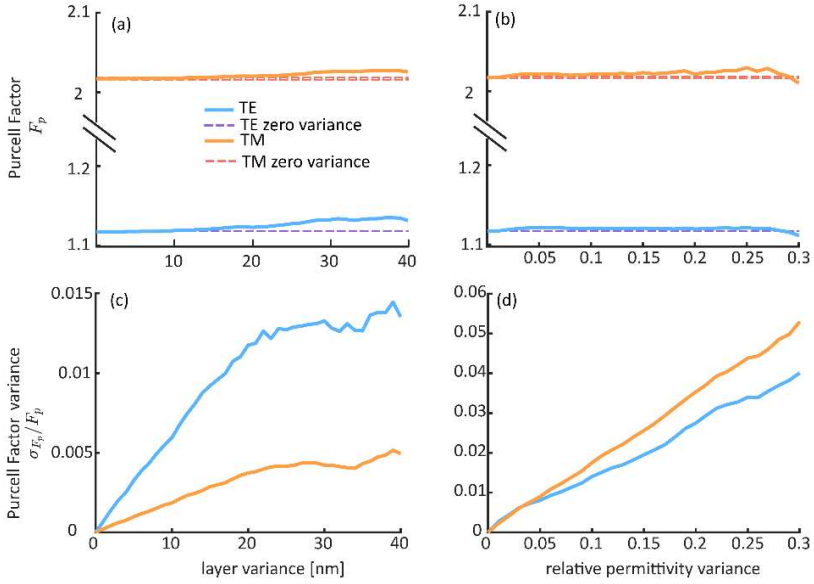

Figure S14: The Purcell factor from an ensemble of structures. These simulations highlight the stability of the resulting Purcell factor, even under large variance in the design parameters. **(a-b)** The mean of the Purcell factor that is calculated from a set of random structures with a variance in the layer thickness (a) and in the relative permittivity (b). **(c-d)** The normalized standard deviation of the Purcell factor that is calculated from a set of random structures with a variance in the layer thickness (c) and in the relative permittivity (d). The fluctuations in the curves, especially for larger variance values, are due to the finite number of structures that we average over.

S7. The effect of scattering on the scintillated signal

This section explains how we introduce scattering to our data analysis, which eventually leads to a good fit between our theory and the experimental results (in Fig. 3c in the main text). The scattering arises from pores and craters on the surface of the structure that are created during the manufacturing process, described in Section 3. There are several different scattering theories (Rayleigh, geometrical or Mie), of which we need to choose one according to the geometrical properties of the pores and to whether the scattering is dependent or independent, and how many scattering processes a single wave may experience.

To answer these questions, we used image processing algorithms on the SEM image to find the scatterers (holes) and extract their locations diameters d, and distance between one another h, see Fig. S15a. By examining over 7000 holes from a total area of 450 μm^2, we determined the geometrical parameters shown in a histograms in Fig. S15b,c. We find that the size parameter $x = \pi d/\lambda$ (where λ is the emission wavelength, 610 nm) is between 0.1 to 20 for almost all holes, which brings the conclusion that the theory that should explain a single scattering process is the Mie theory.

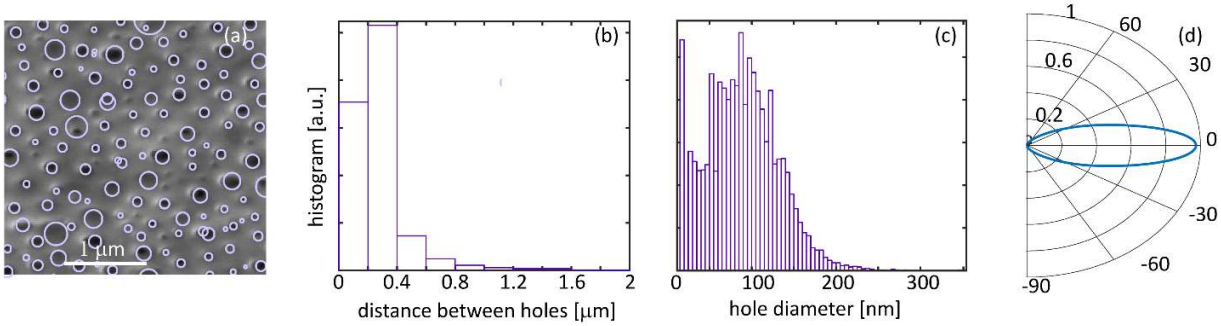

Figure S15: Our method for extracting the simulation parameters from the SEM image. The scattering function (using the Mie theory) is extracted using automated image processing to identify the distribution of defects. **(a)** A zoom-in of the SEM image of the NS top surface (full image at Fig. S9b). We use an image processing algorithm to find the holes (purple). **(b)** The histogram of the distance between holes, showing a Poissonian distribution with mean value of 0.3 μm. **(c)** The histogram of the hole diameter. **(d)** The scattering function from Eq. (S9) that we calculate according to the Mie theory from the histogram data in (b) and (c).

Using the Mie theory, we calculate the scattering and extinction cross sections for each one of the holes

$$\sigma_{\text{scat},j} = \frac{\lambda^2}{2\pi}\sum_{n=1}^{\infty}(2n+1)\left(\left|a_{n,j}^2\right| + \left|b_{n,j}^2\right|\right) \; ; \; \sigma_{\text{ext},j} = \frac{\lambda^2}{2\pi}\sum_{n=1}^{\infty}(2n+1)Re\left(a_{n,j} + b_{n,j}\right) \qquad \text{(S8)}$$

where $a_{n,j} = \frac{m\psi_n(mx_j)\psi_n'(x_j) - \psi_n(x_j)\psi_n'(mx_j)}{m\psi_n(mx_j)\xi_n'(x) - \xi_n(x_j)\psi_n'(mx_j)}$ and $b_{n,j} = \frac{\psi_n(mx_j)\psi_n'(x_j) - m\psi_n(x_j)\psi_n'(mx_j)}{\psi_n(mx_j)\xi_n'(x_j) - m\xi_n(x_j)\psi_n'(mx_j)}$ with $m = \frac{n_1}{n_2}$ being the ratio between the refractive indexes of the holes and the medium respectively, the functions $\psi_n, \xi_n, \psi_n', \xi_n'$ are the Riccati-Bessel functions and their first derivatives, respectively, and $x_j = \frac{\pi d_j}{\lambda}$ is the size parameter of the j'th hole. Once we have all the cross sections, we determine that each emitted wave experience at most only a single scattering event from its emission until its detection because the ratio between $\sum_j \sigma_{\text{ext},j}$ and the total examined area is much smaller than 0.1. Finally, according to the criteria in Ref. (53) that the scattering is independent since $\frac{h}{d} \cong 3 > 0.4$ and $\frac{h}{\lambda} \cong 0.6 > 0.3$.

Then, we calculate the scattering coefficient which presented in Fig. S15d through

$$S(\theta) = \rho\sum_j \sigma_{\text{scat},j} f_j(\theta) \qquad \text{(S9)}$$

where ρ is the number of holes per unit area and $f(\theta)$ is the scattering angular distribution as derived from the Mie theory and calculated by

$$f_j(\theta) = \frac{|S_1(\theta)|^2 + |S_2(\theta)|^2}{\int_0^{\pi}(|S_1(\theta)|^2 + |S_2(\theta)|^2)\sin(\theta)\,d\theta}$$

Where $S_1(\theta) = \sum_{n=1}^{\infty}\frac{2n+1}{n(n+1)}\{a_{n,j}\frac{1}{\sin(\theta)}P_n^1(\cos(\theta)) + b_{n,j}\frac{d}{d\theta}P_n^1(\cos(\theta))\}$ and $S_2(\theta) = \sum_{n=1}^{\infty}\frac{2n+1}{n(n+1)}\{b_{n,j}\frac{1}{\sin(\theta)}P_n^1(\cos(\theta)) + a_{n,j}\frac{d}{d\theta}P_n^1(\cos(\theta))\}$, with P_n^1 being the associated Legendre polynomial of degree n and order 1.

Finally, to calculate the total Purcell factor that includes scattering $F_{p,tot}(\theta)$, we used the following model:

$$F_{p,\mathrm{tot}}(\theta) = (1-\alpha)F_p(\theta) + \alpha F_p(\theta) * S(\theta) \tag{S10}$$

where α is defined as the ratio between the total area of the holes and the area of the layer, F_p is the ensemble average Purcell factor without scattering, and * denotes convolution.

S8. Calculating the light yield

In this section, we bring the calculation of the light yield of our Purcell enhanced scintillator and compare it to the light yield of LYSO. We reach this finding through a comparison of the scintillated signal that we measure as a result of similar X-ray CW excitation between a bulk LYSO, the NS scintillator, and the Lu_2O_3:Eu-Bi homogeneous sample. In Fig. S16a, we show the scintillated spectrum that was measured for all three samples, where the integration time of the LYSO was 11 sec and the integration time of the homogeneous sample and the NS samples was 61 sec. Then, when summing up all counts in the spectra and dividing by the integration time of each measurement, we find the number of counts per second of illumination in each sample is S_{LYSO}, S_{NS}, S_{Homog}. We find that these ratios are $\frac{S_{\mathrm{LYSO}}}{S_{\mathrm{NS}}} = 16.8$, $\frac{S_{\mathrm{LYSO}}}{S_{\mathrm{Homog}}} = 29.95$, and $\frac{S_{\mathrm{NS}}}{S_{\mathrm{Homog}}} = 1.78$.

Now, we know that the LYSO is thick enough to stop all of the X-ray radiation, but the NS and the homogenous sample are not. To calculate how much of the X-ray was stopped by the NS, we look at the X-ray mass attenuation coefficient of the Lu_2O_3 using the formula[6]

$$\frac{\mu}{\rho} = \sum_i w_i \left(\frac{\mu}{\rho}\right)_i \tag{S11}$$

where $\left(\frac{\mu}{\rho}\right)_i$ is the X-ray mass attenuation coefficient of element i and w_i is its weight fraction in the compound mixture, ρ is the density of Lu_2O_3 ($9.42\ \frac{\mathrm{gr}}{\mathrm{cm}^3}$) and $\frac{1}{\mu(E)}$ will be the typical distance for stopping X-ray of energy E. By plugging $\frac{\mu}{\rho}$ of Lutetium and of Oxide[7], we can find the typical distance per illumination energy, shown in Fig S16b.

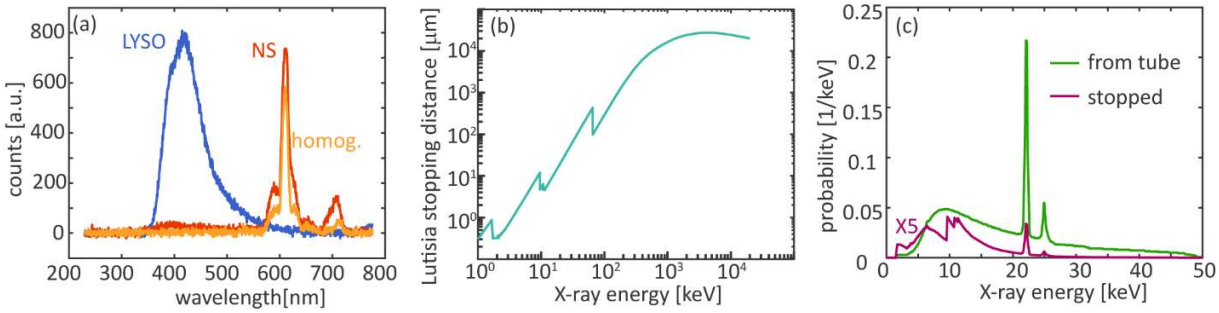

Figure S16: Finding the stopping power of the nanophotonic scintillator for the light-yield calculation. (a) Scintillated spectrum for the different samples, where the LYSO signal had an integration time of 61 sec, while the two other samples 11 sec. (b) Stopping distance of Lu_2O_3 as calculated from Eq. (S11). (c) The X-ray spectrum as emitted from the tube (green, normalized so that its integration over energy is 1), and the X-ray spectrum that is stopped by the sample (purple, the summation over energy provides the total stopping probability).

Given the stopping distance, we calculate the probability that an X-ray photon of energy E is stopped, $p(E) = 1 - e^{d\mu(E)}$, where d is the Lu_2O_3 thickness in our sample, which is (on average) 880 nm. We multiply the original X-ray spectrum with this probability (shown in Fig. S16c), to find the spectrum of the stopped X-rays and the percentage that any particular X-ray photon is stopped. We find that our sample stops 8% of the radiation that arrives to it from our source, with an average energy of $\langle E_{\mathrm{X-ray,NS}} \rangle$ =11.65 keV (which is smaller compared to an average of $\langle E_{\mathrm{X-ray,LYSO}} \rangle = 18.91$ keV of the X-ray source).

Given the X-ray flux $F_{\mathrm{X-ray}}$ (number of X-ray photons per seconds), we calculate the light yields of the LYSO and NS scintillators

$$LY_{\mathrm{LYSO}} = \frac{S_{\mathrm{LYSO}}}{F_{\mathrm{X-ray}} \langle E_{\mathrm{X-ray,LYSO}} \rangle} \; ; \; LY_{PhC} = \frac{S_{\mathrm{NS}}}{0.08 F_{\mathrm{X-ray}} \langle E_{\mathrm{X-ray,NS}} \rangle} \qquad (S12)$$

where we have a 0.08 factor in the LY_{PhC} denominator because only 8% of the X-ray photons were stopped by the Lu_2O_3 sample. Since we do not know the exact flux in our system, we can compare the ratio

$$\frac{LY_{\mathrm{NS}}}{LY_{\mathrm{LYSO}}} = \frac{S_{\mathrm{NS}}}{S_{\mathrm{LYSO}}} \frac{E_{\mathrm{X-ray,LYSO}}}{0.08E_{\mathrm{X-ra\ ,NS}}} = 1.2$$

That is, after normalization by the number and the energy of the stopped X-ray photons, the NS scintillator has a light yield which is $S_{\mathrm{NS}}/S_{\mathrm{LYSO}} = 1.2$ times better than the light yield of LYSO. A similar calculation shows that the light yield of the Lu_2O_3 homogeneous sample is smaller than that of LYSO, and the factor is $S_{\mathrm{Homog}}/S_{\mathrm{LYSO}} = 0.66$. We can find the absolute number of LY_{NS} by taking LY_{LYSO} from the literature. Under similar X-ray illumination, LY_{LYSO} is 32,200 ph/MeV (54), so that eventually we have $LY_{\mathrm{NS}} = 38{,}000$ ph/MeV, and $LY_{\mathrm{TF}} = 21{,}300$ ph/MeV (which is smaller than the value found in the literature for the same scintillator fabricated using sol-gel[9], as expected by the far from perfect sample quality).

S9. *Q*-Factor analysis for Purcell nanophotonic scintillators

In this section and in Fig. S17, we present the influence of the *Q*-factor on the performance of the scintillator presented in our manuscript, by varying the number of layers in the photonic crystal (since the *Q*-factor increases with the number of layers). We show the transmission coefficient of the whole structure, which depends on the *Q*-factor of each mode through the spectral width of each peak (each mode). A low-*Q* design (e.g., $Q \sim 10$, 8-layers) enables a specific mode to cover most of the wide emission spectrum of our scintillator so that all emitters emit light, though the emission rate enhancement is expected to be limited. In contrast, a higher-*Q* design (e.g., $Q \sim 60$, 50-layer structure) enables a much higher emission rate for a few of the modes due to their high-*Q*, but at the expense of emission rate reduction for other modes, limiting the overall light-yield. Notably, the structure optimization for scintillation applications is a challenging problem that some of the authors confronted theoretically in a recent paper (23).

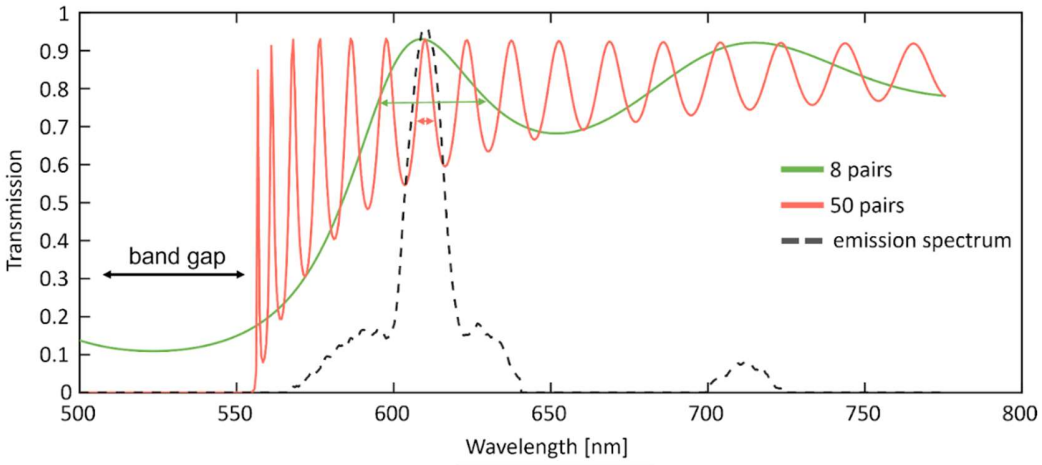

Figure S17. The *Q*-factor of specific optical modes, described by the transmission at 20° from nanophotonic Purcell scintillators with 8 and 50 pairs. The thicknesses of the layers are 96.5 nm and 68 nm. To enhance the emission, the peak of the transmission is aligned with the peak of the emission spectrum (dashed line). The optical modes on the emission spectra peak achieve *Q*-factor of 18.4 and 101.7 in 8 and 50 pairs structures, respectively. Since the emission spectrum covers more than a single emission mode for the 50-layer structure, part of the emission would lie in a dip, creating an unwanted emission reduction.

S10. Additional nanophotonic control with surface photonic crystals

In this section, we provide further numerical simulations showing how blazed gratings could be used to enhance scintillation outcoupling in Fig. S18. The calculations are performed using the Lorentz-reciprocity-based framework for structures with similar geometrical parameters as those measured experimentally in our work. We compare the scintillation emission of a multilayer scintillator to that of a multilayer scintillator with an etched photonic crystal on its top surface, a design known to enhance scintillation outcoupling.

We show that this type of design (which could be readily fabricated with focused ion beam lithography on top of our multilayer samples) would yield a further 5x enhancement in light outcoupling (to the detector) and can also be used to control the outcoupling angle (in this case, the photonic crystal allows outcoupling at a shallower angle than the maximum emission angle of

~25°). This finding highlights the potential for an additional nanophotonic control by adding surface photonic crystals on top of multilayer nanophotonic scintillators.

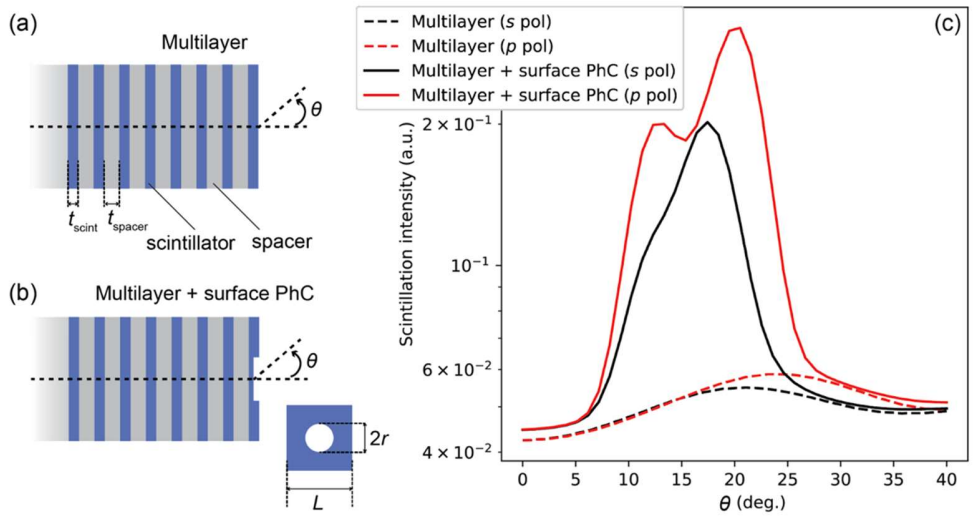

Figure S18: Additional nanophotonic control with surface photonic crystals. (a) Schematic of a multilayer nanophotonic scintillator. (b) Schematic of multilayer nanophotonic scintillator with an etched photonic crystal in the top scintillating layer. (c) Corresponding scintillation emission intensity for different polarizations, showing a further order-of-magnitude enhancement due to nanophotonic patterning. Parameters for this simulation are: t_{scint} = 70 nm, t_{spacer} = 100 nm, r = 125 nm, L = 500 nm, and an etch depth of 20 nm. The angular response in (c) is smoothened on the scale of ~ 4° to eliminate spurious features from high-Q resonances (which would typically be eliminated naturally in experiments due to the presence of disorder).

REFERENCES AND NOTES

1. C. W. van Eijk, Inorganic scintillators in medical imaging detectors. *Nucl. Instrum. Methods Phys. Res. A* **509**, 17–25 (2003).

2. P. Moskal, T. Bednarski, P. Białas, M. Ciszewska, E. Czerwiński, A. Heczko, M. Kajetanowicz, Ł. Kapłon, A. Kochanowski, G. Konopka-Cupiał, G. Korcyl, W. Krzemień, K. Łojek, J. Majewski, W. Migdał, M. Molenda, S. Niedźwiecki, M. Pałka, Z. Rudy, P. Salabura, M. Silarski, A. Słomski, J. Smyrski, J. Zdebik, M. Zieliński, TOF-PET detector concept based on organic scintillators. *Nucl. Med. Rev.* **15**, C81–C84 (2013).

3. R. A. Cecil, B. D. Anderson, R. Madey, Improved predections of neutron detection efficiency for hydrocarbon scintillators from 1 MeV to about 300 MeV. *Nucl. Instrum. Methods* **161**, 439–447 (1979).

4. G. Knoll, *Radiation Detection and Measurement* (Wiley, 2010).

5. P. Lecoq, A. Gektin, M. Korzhik, *Inorganic Scintillators for Detector Systems* (Springer, 2017).

6. P. Lecoq, Development of new scintillators for medical applications. *Nucl. Instrum. Methods Phys. Res. A* **809**, 130–139 (2016).

7. C. Dujardin, E. Auffray, E. Bourret-Courchesne, P. Dorenbos, P. Lecoq, M. Nikl, A. N. Vasil'ev, A. Yoshikawa, R. Y. Zhu, Needs, trends, and advances in inorganic scintillators. *IEEE Trans. Nucl. Sci.* **65**, 1977–1997 (2018).

8. F. Maddalena, L. Tjahjana, A. Z. Xie, Arramel, S. Zeng, H. Wang, P. Coquet, W. Drozdowski, C. Dujardin, C. Dang, M. Birowosuto, Inorganic, organic, and perovskite halides with nanotechnology for high–light yield X- and γ-ray scintillators. *Crystals* **9**, 88 (2019).

9. J. W. Cates, C. S. Levin, Evaluation of a clinical TOF-PET detector design that achieves ≤100 ps coincidence time resolution. *Phys. Med. Biol.* **63**, 115011 (2018).

10. P. Lecoq, Pushing the limits in time-of-flight PET imaging. *IEEE Trans. Radiat. Plasma Med. Sci.* **1**, 473–485 (2017).

11. F. Gramuglia, S. Frasca, E. Ripiccini, E. Venialgo, V. Gâté, H. Kadiri, N. Descharmes, D. Turover, E. Charbon, C. Bruschini, Light extraction enhancement techniques for inorganic scintillators. *Crystals* **11**, 362 (2021).

12. O. Svenonius, A. Sahlholm, P. Wiklund, J. Linnros, Performance of an X-ray imaging detector based on a structured scintillator. *Nucl. Instrum. Methods Phys. Res. A* **607**, 138–140 (2009).

13. M. Kronberger, E. Auffray, P. Lecoq, Probing the concepts of photonic crystals on scintillating materials. *IEEE Trans. Nucl. Sci.* **55**, 1102–1106 (2008).

14. A. Knapitsch, P. Lecoq, Review on photonic crystal coatings for scintillators. *Int. J. Mod. Phys. A* **29**, 1430070 (2014).

15. C. Roques-Carmes, N. Rivera, A. Ghorashi, S. E. Kooi, Y. Yang, Z. Lin, J. Beroz, A. Massuda, J. Sloan, N. Romeo, Y. Yu, J. D. Joannopoulos, I. Kaminer, S. G. Johnson, M. Soljačić, A framework for scintillation in nanophotonics. *Science* **375**, eabm9293 (2022).

16. Y. Kurman, A. Shultzman, O. Segal, A. Pick, I. Kaminer, Photonic-crystal scintillators: Molding the flow of light to enhance X-ray and γ-ray detection. *Phys. Rev. Lett.* **125**, 040801 (2020).

17. W. Ye, Z. Yong, M. Go, D. Kowal, F. Maddalena, L. Tjahjana, H. Wang, A. Arramel, C. Dujardin, M. D. Birowosuto, L. J. Wong, The nanoplasmonic purcell effect in ultrafast and high-light-yield perovskite scintillators. *Adv. Mater.* **36**, 2309410 (2024).

18. W. Ye, G. Bizarri, M. D. Birowosuto, L. J. Wong, Enhancing large-area scintillator detection with photonic crystal cavities. *ACS Photonics* **9**, 3917–3925 (2022).

19. E. M. Purcell, Spontaneous emission probabilities at radio frequencies. *Phys. Rev.* **69**, 839 (1946).

20. T. Baba, T. Hamano, F. Koyama, K. Iga, Spontaneous emission factor of a microcavity DBR surface-emitting laser. *IEEE J. Quantum Electron.* **27**, 1347–1358 (1991).

21. E. F. Schubert, Y.-H. Wang, A. Y. Cho, L.-W. Tu, G. J. Zydzik, Resonant cavity light-emitting diode. *Appl. Phys. Lett.* **60**, 921–923 (1992).

22. D. Englund, D. Fattal, E. Waks, G. Solomon, B. Zhang, T. Nakaoka, Y. Arakawa, Y. Yamamoto, J. Vučković, Controlling the spontaneous emission rate of single quantum dots in a two-dimensional photonic crystal. *Phys. Rev. Lett.* **95**, 013904 (2005).

23. E. J. R. Vesseur, R. de Waele, M. Kuttge, A. Polman, Direct observation of plasmonic modes in Au nanowires using high-resolution cathodoluminescence spectroscopy. *Nano Lett.* **7**, 2843–2846 (2007).

24. A. Losquin, M. Kociak, Link between cathodoluminescence and electron energy loss spectroscopy and the radiative and full electromagnetic local density of states. *ACS Photonics* **2**, 1619–1627 (2015).

25. M. Boroditsky, R. Vrijen, T. F. Krauss, R. Coccioli, R. Bhat, E. Yablonovitch, Spontaneous emission extraction and Purcell enhancement from thin-film 2-D photonic crystals. *J. Lightwave Technol.* **17**, 2096–2112 (1999).

26. P. Lodahl, A. F. van Driel, I. S. Nikolaev, A. Irman, K. Overgaag, D. Vanmaekelbergh, W. L. Vos, Controlling the dynamics of spontaneous emission from quantum dots by photonic crystals. *Nature* **430**, 654–657 (2004).

27. H. Aouani, O. Mahboub, E. Devaux, H. Rigneault, T. W. Ebbesen, J. Wenger, Large molecular fluorescence enhancement by a nanoaperture with plasmonic corrugations. *Opt. Exp.* **19**, 13056–13062 (2011).

28. G. Konstantinou, P. Lecoq, J. M. Benlloch, A. J. Gonzalez, Metascintillators for ultrafast gamma detectors: A review of current state and future perspectives. *IEEE Trans. Radiat. Plasma Med. Sci.* **6**, 5–15 (2022).

29. L. Novotny, B. Hecht, *Principles of Nano-Optics* (Cambridge Univ. Press, ed. 2, 2012).

30. A. Shultzman, O. Segal, Y. Kurman, C. Roques-Carmes, I. Kaminer, Enhanced imaging using inverse design of nanophotonic scintillators. *Adv. Opt. Mater.* **11**, 2202318 (2023).

31. Y. Wang, T. Yang, M. T. Tuominen, M. Achermann, Radiative rate enhancements in ensembles of hybrid metal-semiconductor nanostructures. *Phys. Rev. Lett.* **102**, 163001 (2009).

32. W. Vogel, D. G. Welsch, *Quantum Optics* (Wiley-VCH, 2006).

33. O. Segal, A. Shultzman, Y. Kurman, I. Kamine, Optimizing the spontaneous-emission of far-UVC phosphors. *Appl. Phys. Lett.* **120**, 231902 (2022).

34. W. C. Chew, *Waves and Fields in Inhomogeneous Media* (IEEE Press, 1995).

35. E. Yablonovitch, Statistical ray optics. *J. Opt. Soc. Am.* **72**, 899 (1982).

36. A. R. Gubaydullin, V. A. Mazlin, K. A. Ivanov, M. A. Kaliteevski, C. Balocco, Angular and positional dependence of Purcell effect for layered metal-dielectric structures. *App. Phys. A* **122**, 425 (2016).

37. O. Segal, A. Shultzman, Y. Kurman, I. Kaminer, Optimizing optical nanostructures for X-ray detection. *AIP Conf. Proc.* **2300**, 020110 (2020).

38. J. D. Joannopoulos, S. G. Johnson, J. N. Winn, R. D. Meade, *Photonic Crystals: Molding the Flow of Light* (Princeton Univ. Press, 2011).

39. A. Szameit, S. Nolte, Discrete optics in femtosecond-laser-written photonic structures. *J. Phys. B At. Mol. Opt. Phys.* **43**, 163001 (2010).

40. F. Niesler, M. Hermatschweiler, Two-photon polymerization—A versatile microfabrication tool. *Laser Tech. J.* **12**, 44–47 (2015).

41. A. Ródenas, M. Gu, G. Corrielli, P. Paiè, S. John, A. K. Kar, R. Osellame, Three-dimensional femtosecond laser nanolithography of crystals. *Nat. Photonics* **13**, 105–109 (2019).

42. R. M. Turtos, S. Gundacker, S. Omelkov, B. Mahler, A. H. Khan, J. Saaring, Z. Meng, A. Vasil'ev, C. Dujardin, M. Kirm, I. Moreels, E. Auffray, P. Lecoq, On the use of CdSe scintillating nanoplatelets as time taggers for high-energy gamma detection. *NPJ 2D Mater. Appl.* **3**, 37 (2019).

43. A. Hospodková, M. Nikl, O. Pacherová, J. Oswald, P. Brůža, D. Pánek, B. Foltynski, E. Hulicius, A. Beitlerová, M. Heuken, InGaN/GaN multiple quantum well for fast scintillation application: Radioluminescence and photoluminescence study. *Nanotechnology* **25**, 455501 (2014).

44. J. M. Nedelec, Sol-gel processing of nanostructured inorganic scintillating materials. *J. Nanomater.* **2007**, 1–8 (2007).

45. W. Kern, J. L. Vossen *Thin Film Processes II* (Elsevier Science, 2012).

46. D. Sengupta, S. Miller, Z. Marton, F. Chin, V. Nagarkar, G. Pratx, Bright Lu_2O_3:Eu thin-film scintillators for high-resolution radioluminescence microscopy. *Adv. Healthc. Mater.* **4**, 2064–2070 (2015).

47. A. M. Ramírez, M. G. Hernández, J. Y. Ávila, A. G. Murillo, F. C. Romo, E. de la Rosa, V. G. Febles, J. R. Miranda, Eu^{3+}, Bi^{3+} codoped Lu_2O_3 nanopowders: Synthesis and luminescent properties. *J. Mater. Res.* **28**, 1365–1371 (2013).

48. H. Kozuka, S. Takenaka, H. Tokita, T. Hirano, Y. Higashi, T. Hamatani, Stress and cracks in gel-derived ceramic coatings and thick film formation. *J. Solgel Sci. Technol.* **26**, 681–686 (2003).

49. C. H. Hsueh, C. R. Luttrell, T. Cui, Thermal stress analyses of multilayered films on substrates and cantilever beams for micro sensors and actuators. *J. Micromech. Microeng.* **16**, 2509–2515 (2006).

50. T. O. L. Sunde, T. Grande, M.-A. Einarsrud, "Modified Pechini synthesis of oxide powders and thin films" in *Handbook of Sol-Gel Science and Technology: Processing, Characterization and Applications* (Springer Nature, 2018), pp. 1089–1118.

51. V. V. Ter-Mikirtychev, “Optical spectroscopy of rare-earth ions in the solid state” in *Encyclopedia of Spectroscopy and Spectrometry* (Elsevier, 2017), pp. 481–491.

52. R. W. Schwartz, T. Schneller, R. Waser, Chemical solution deposition of electronic oxide films. *Comptes Rendus Chim.* **7**, 433–461 (2004).

53. J. Wang, “Angle dependent light scattering of functional nanoparticle composites,” thesis, Acta Universitatis Upsaliensis (2019).

54. T. Kimble, M. Chou, B. H. T. Chai, “Scintillation properties of LYSO crystals” in *2002 IEEE Nuclear Science Symposium Conference Record* (IEEE, 2002), pp. 1434–1437.